Preliminary optical and thermal design of a 600 kWh direct absorption molten salt receiver/storage system

Benjamin Grange [a, *], Vikas Kumar [a], Antoni Gil [b], Miguel Diago [a], Peter R. Armstrong [a], Alexander Slocum [b], and Nicolas Calvet [a]

[a] Institute Center for Energy (iEnergy), Department of Mechanical and Materials Engineering, Masdar Institute of Science and Technology, Masdar City, P.O. Box 54224, Abu Dhabi, United Arab Emirates.

[b] Department of Mechanical Engineering, Massachussets Institute of Technology, 77 Massachussets Ave, Cambridge, MA 02139, United States of America.

Abstract

A concentrated solar power beam-down tower focuses its energy directly into a single-tank molten salt volumetric receiver that also acts as a thermal energy storage unit. The system is being developed in connection with the CSPonD Demo (Concentrated Solar Power on Demand Demonstration) at the Masdar Institute of Science and Technology in partnership with MIT.. The relatively small angle subtended by rays emanating from the central reflector of a beam down optical system, together with the nature of solar energy absorption within the volumetric receiver, make use of a compound parabolic concentrator (CPC) or CPC-like final optical element (FOE) attractive. An effective concentration of about 4-5 can be achieved to increase solar flux at the tank aperture from 150 to 600 suns. This paper describes preliminary designs of the CPC and tank/receiver. Optical simulations reveal that, for a given solar incident power at the tank aperture, a conical final concentrator design produces a more uniform flux distribution with better axial alignment (lower average horizontal component) of rays at its outlet, compared to a conventional CPC of revolution. However, the cone may require a larger outlet radius, leading to higher thermal losses through the tank aperture. With the current design of the tank, the losses through the walls, as well as the convective losses through the aperture during day time, correspond to 4.5 % of the thermal capacity.

Selection and/or peer-review under responsibility of ICAE.

Keywords: Thermal energy storage; concentrated solar power; direct absorption molten salt; beam-down tower; final optical element; ray-tracing.

1. Introduction

Concentrating solar power (CSP) systems that use thermal energy storage (TES) to provide dispatchability [1, 2, 3] do so at costs much lower than than the costs of electro-chemical storage options currently available to make wind and PV power dispatchable. Nevertheless, opportunities exist to further improve TES implementations in terms of transport energy and heat exchanger exergy losses. To effect these improvements, a hot-tank volumetric receiver scheme that requires a window on top of it to suppress convection losses was proposed [4]. The CSPonD single-tank molten salt TES which also serves as a low-cost volumetric receiver was developed [5, 6]. To improve upon the natural thermocline effect, an insulated divider plate is positioned within the tank to promote thermal stratification between hot and cold salt volumes [7]. In contrast to conventional solar tower systems, the CSPonD receiver must be built on the ground necessitating a hillside heliostat field [8] and hybrid cavity receiver design [9], or a beam-down optical system [10]. One such system, the Masdar Institute Beam Down Optical Experiment (BDOE) is a 100 kW_{th} demonstration plant that was initially (2009-2011) operated to prove and gain experience with novel beam-down optical elements [11, 12]. To achieve high concentration ratio with beam-down towers while reducing spillage and thermal losses, a CPC or final optical element is essential. This element has already been investigated either with collimated beams with uniform radiation [13, 14] or with non-symmetric input beam [15]. Several designs have been analyzed such as CPC approximation and cone [15], polygonal or truncated CPC [16, 17]. However with the BDOE specific beam distribution and the molten salt direct absorption receiver / TES tank on the ground, the optimization of the final optical element is unique and needs to be carried out. In this paper we describe the design of a continuous 25 kW_{th} CSPonD system using the BDOE with modified optics as a source of concentrated radiation to test a 600 kWh directly irradiated molten salt TES operating between 250ºC and 550ºC [18].

---

* Corresponding author. Dr. Benjamin Grange. Tel.: +971-2810-9350; fax: +971-2810-9901; E-mail address: bgrange@masdar.ac.ae.

This paper was presented at the 7th International Conference on Applied Energy (ICAE2015), March 28-31, 2015, Abu Dhabi, UAE (Original paper title: " Preliminary optical, thermal and structural design of a 100 kW_{th} CSPonD beam-down on-sun demonstration plant" and Paper No.: 630)

2. Optical analysis and design

2.1. Heliostat field and central reflector description

The BDOE heliostat field comprises 33 ganged-type heliostats each of 8.505 m^2 reflector area representing a total aperture area of 280.7 m^2. Heliostats are arranged in three circles around the tower with an outer circle radius of 18 m. Each heliostat comprises 42 individual mirror facets arranged in three banks presented in Fig. 1(a). The elevation and azimuth angles are calculated to reflect the incident Direct Normal Irradiation (DNI) to a focal point above the top of the tower (Fig. 2). A sun sensor aimed at the central facet of each heliostat provides reflected ray feedback for positioning each heliostat such that the sun's image as viewed from z = 20.3 m is always centred in the control mirror.
A central reflector (CR), mounted at 16 m on the central tower, provides a second optical stage consisting of three multi-faceted rings, as shown in Fig. 1(b). The rings of the CR correspond to the heliostats rings on the ground such that each secondary mirror facet is used for a specific heliostat. The overall arrangement is shown in Fig. 1(c).

(a) (b) (c)

Fig. 1. Solar beam down components (a) typical heliostat [11]; (b) central reflectors, (c) view of central tower in heliostat field.

The CR facets, which are manually adjustable but stationary in operation, were initially canted so as to reflect radiation to a solar receiver located 2 m above the ground directly below the CR as shown in Fig. 2. The receiver of the original BDOE was a 16 ft x 16 ft (4.88 m x 4.88 m) projection screen comprising 256 white, near-lambertian ceramic tiles, used for photogrammetric evaluation of the concentrated beam [19].

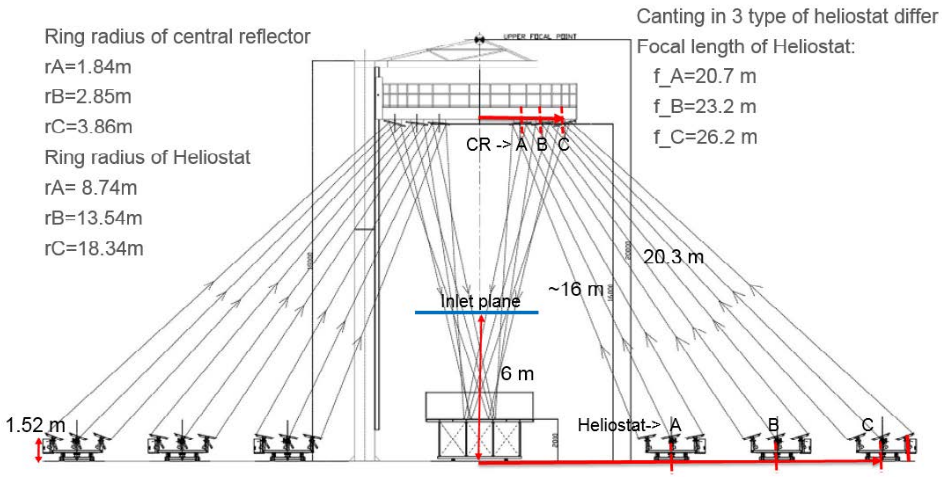

Fig. 2. Schematic of Masdar Institute BDOE showing its essential dimensions and the projection screen used for flux mapping

2.2. Modification to CR and addition of 3rd optical stage

The overall efficiency of a CSP plant involves trade-offs between optical (several reflector stages), thermal (receiver), and thermodynamic (power block) efficiencies. Higher thermal and thermodynamic efficiencies may be achieved by higher concentrations at the expense of optical efficiency.
With the existing heliostats field and CR geometry (Fig. 2), a flux of about 150 suns is realized with solar zenith angles less than about 40°. The ~25° half-angle of CR edge rays (Fig. 2) means that an additional concentration of about 4-5 can be achieved by introducing a final non-imaging optical element. This will increase optical losses but reduce thermal losses by reducing the aperture area.
Monte-Carlo ray tracing [20] was used to evaluate performance of various CR canting angles and final optical element (FOE) geometries. The BDOE solid model is shown with a conical FOE at 6 m elevation (inlet aperture) in Fig. 3. All the simulations were processed in TracePro 7.5.7 running on a Windows 7-64 bit computer setup (Dell T7610, 64 GB

RAM, 2 Intel Xeon processors E5-2650 v2 at 2.60 GHz). The sun was modelled as a circular source of radius 30 m in which the ray origins were arranged in 1420 concentric rings producing 6,044,941 rays. The solar angular profile was included in the simulations. All HS and CR facets were modelled as perfectly flat mirrors.

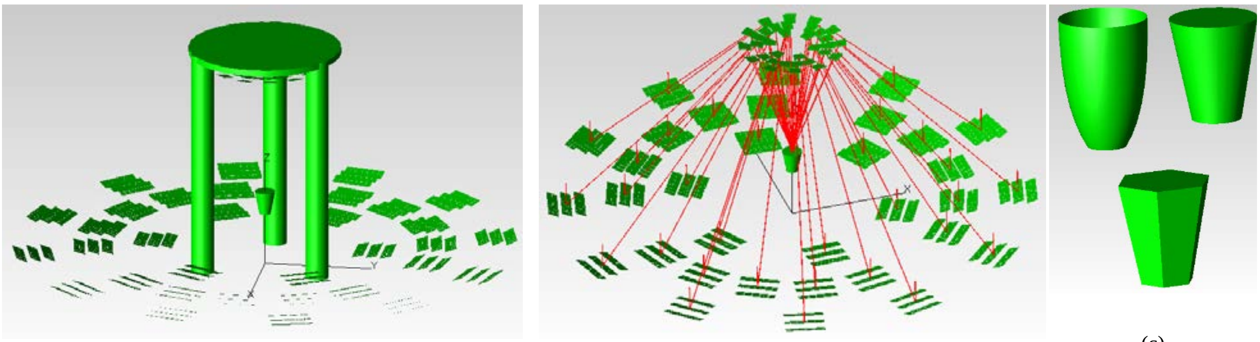

(a) (b) (c)

Fig. 3. BDOE models (a) reflective and opaque surfaces; (b) reflective surfaces only; (c) CPC, cone and faceted cone

The CR mirrors shown in Figure 3 are canted more toward the z-axis than in Fig. 2 to produce maximum concentration at a FOE inlet aperture raised from 2 m to 6 m. Elevation of the inlet aperture is a key parameter for certain FOE geometries such as the compound parabolic concentrator (CPC) of revolution [21, 22]. For a CPC FOE, the optimal CR cantings result in all 33 CR facet central reflected rays intersecting the z-axis at the inlet aperture plane. CR canting also affects the angular distribution, as well as spatial distribution, of rays incident on the inlet plane. We consider both surface-of-revolution FOE's and their faceted counterparts as shown in Fig. 3c.

2.3. Optical simulation results for BDOE with different CR canting angles

The beam down optics are modelled in two steps. The heliostat field and CR are simulated first to produce a ray vector file at an intermediate plane above the highest reasonable inlet aperture plane as shown at 6 m in Fig. 2. An intermediate-plane ray vector file can be produced for any given sun position and CR canting. We define optical efficiency of the heliostat-CR subsystem as

$$\eta_{optical} = \frac{\dot{Q}_{In,FOE}}{\dot{Q}_{HF}} \tag{1}$$

where $\dot{Q}_{In,FOE}$ is the power available at the inlet plane of the final optical element and $\dot{Q}_{HF}$ is the incident power on heliostats taken one by one without shading, to account for the overall cosine efficiency (cf. orange plot in Fig. 4) according to:

$$\dot{Q}_{HF} = A_{HS} DNI \sum_{i=1}^{33} \cos(\theta_i) \tag{2}$$

where A_{HS} is the reflective surface of a single heliostat, *DNI* is the Direct Normal Irradiance and θ_i is direct beam incident angle on i^{th} heliostat for the sun position in question.

Thus $\eta_{optical}$ accounts for shading, blocking, heliostat reflection loss, CR spillage, CR reflection loss, and FOE spillage. With the FOE inlet situated 6 m above grade, the optical efficiency of the heliostat-CR subsystem varies from 77 % to 22 % depending mainly on the solar zenith angle.

The results of heliostat-CR ray-tracing simulations for zenith angles from 5° to 85° may be used to produce subsystem efficiency curves like those shown in Fig. 4.

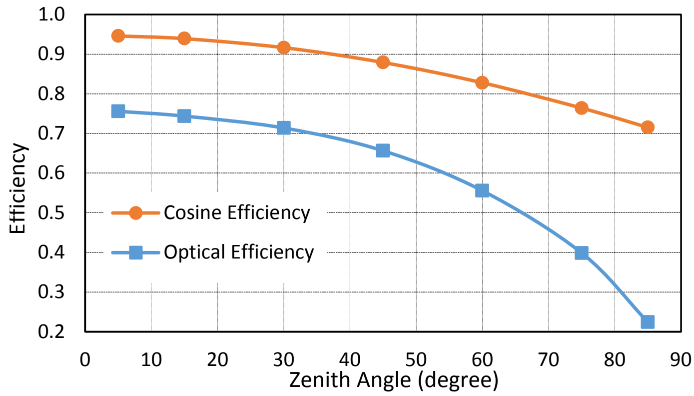

Fig. 4. Heliostat-CR optical losses: reflectance, blocking, shading, spillage

2.4. Optical simulation results for different FOE geometries

Final optical element efficiency is usually given as outlet power divided by inlet power. However, in the case of a molten salt volume receiver, angular distribution of outlet flux has a significant impact on receiver "window" reflection loss. It may also be important to consider uniformity of flux (areal distribution) over the outlet aperture. Results for the 21st of June at noon (DNI = 796 W/m²) and at 10 am (DNI = 724 W/m²), Figures 5 and 6, show that flux distributions typically have good radial symmetry (θ_z = 1°) at noon but are slightly skewed (θ_z = 27°) at 10 am.

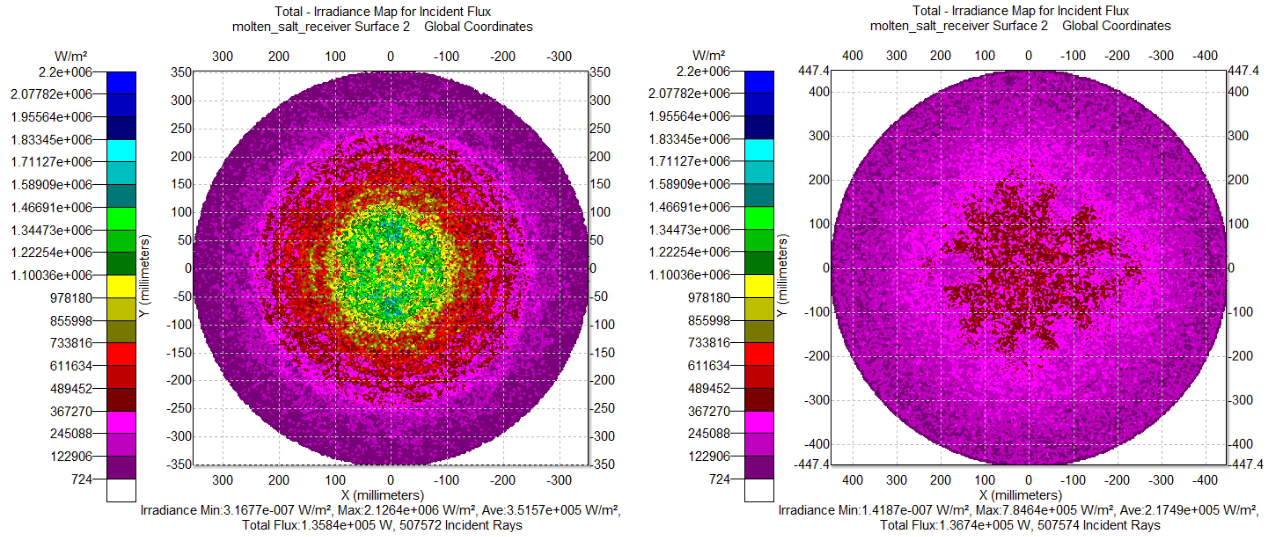

Fig. 5. Outlet aperture flux maps at noon June 21st for two final optical elements: CPC on left and conical FOE on right.

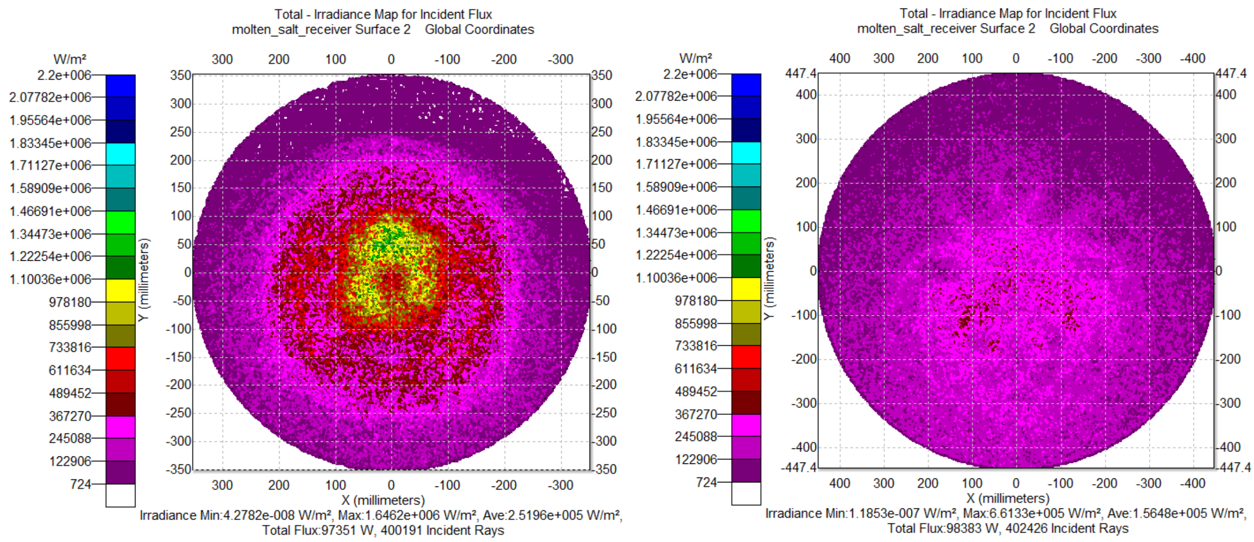

Fig. 6. Outlet aperture flux maps at 10am June 21st for two final optical elements: CPC on left and conical FOE on right.

To ease the manufacture and the possible maintenance of the FOE, the optical performance of a 6 faceted conical FOE was also investigated. Inlet and exit radii are defined to get the same inlet and exit areas as the conical FOE. Figures 7 and 8, show the flux distributions with a smaller colormap range. It is interesting that although a 6 faceted FOE is very slightly less efficient, it produces a more uniform flux.

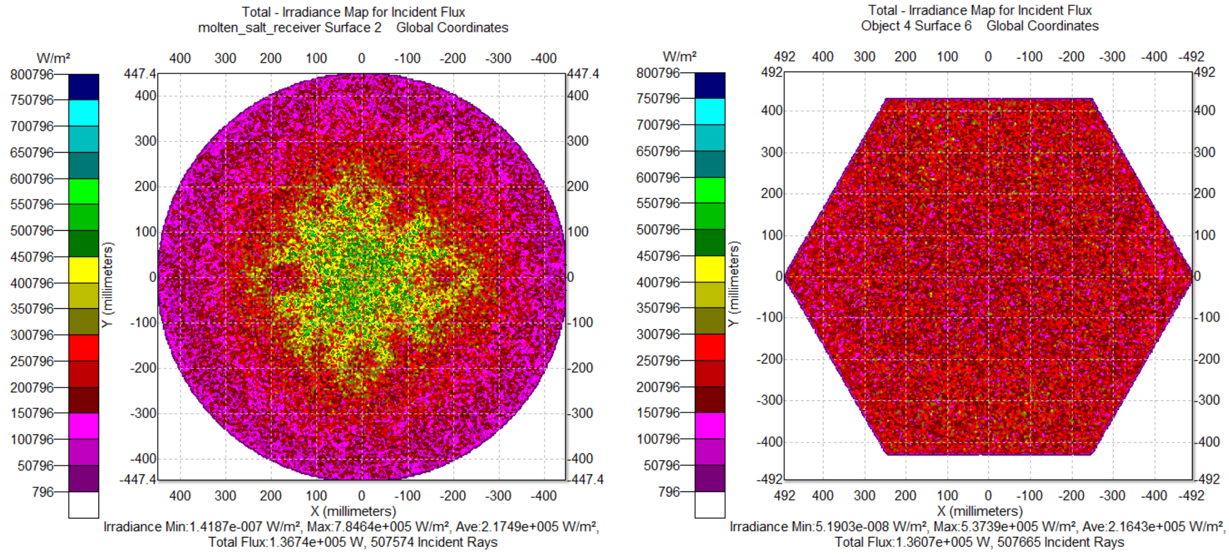

Fig. 7. Outlet aperture flux maps at noon June 21st for two final optical elements: conical FOE on left and 6 faceted conical FOE on right.

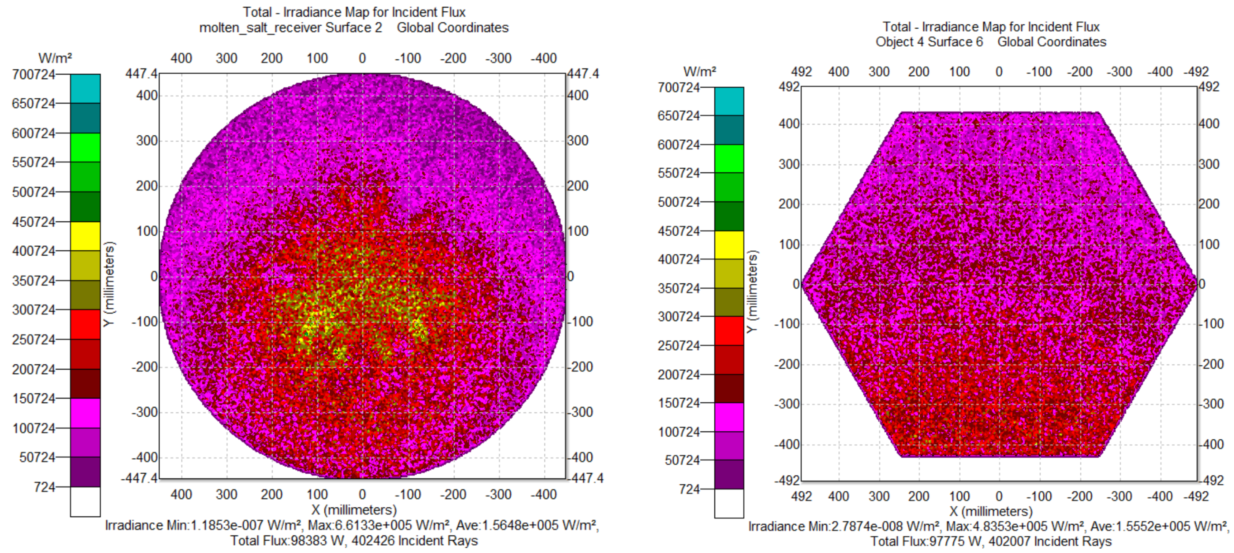

Fig. 8. Outlet aperture flux maps at 10 am June 21st for two final optical elements: conical FOE on left and 6 faceted conical FOE on right.

FOE ray-tracing results are summarized in terms of total flux in Table 1. The parameterizations of Fig. 4 and Table 1 enable hour-by-hour simulations and system-level optimal control with reasonable computational effort.

Table 1. Final optical element performance for a CPC and a cone

	CPC		**Cone**		**6 faceted cone**	
Half angle (degree)	26		34		34	
Inlet Radius (m)	0.8		0.8		0.76	
Exit Radius (m)	0.35		0.45		0.43	
Length (m)	2.36		1.85		1.85	
Time (24 h clock)	12	10	12	10	12	10
FOE Inlet (kW)	143.2	104.1	143.2	104.1	142.6	103
FOE Outlet (kW)	135.8	97.4	136.8	98.4	136.1	97.8
Salt Input (kW)	128.4	91.7	131.8	94.5	131.2	94

2.5. Confidence interval

Monte-Carlo ray tracing produces millions of source rays with angular and spatial distributions determined by a pseudo-random number algorithm. We use such a ray source to model the sun. Thus the outcome of a given simulation depends on the number used to seed the random number generator.

A simulation at solar noon, June 21st, 2011, was repeated 35 times using different random number seeds. Both the total power and maximum flux at the inlet of the CPC were determined and processed to obtain their mean values and estimated standard deviations (confidence interval, CI = 65%). It was found that the total power reaching the CPC inlet was $1.369\times10^5 \pm 81.24$ W and the maximum flux was $3.731\times10^5 \pm 1.203\times10^4$ W/m^2.

3. TES tank design

3.1. Description of the TES system

The TES system linked to the CPC is designed to store 400 kWh and allow a constant nominal power of 25 kW over 24 hours per day. During the day (charging period of 8 hours) the storage system is designed to generate 25 kW and store the energy necessary to keep the system at full load operation during night (discharging period of 16 hours), resulting in a total energy of 600 kWh.

The system consists of a SS316 cylindrical tank containing 2990 kg of Solar Salt (60 wt.% $NaNO_3$ + 40 wt.% KNO_3) as storage material [23]. The salt is heated up from 250ºC to 550ºC by the solar incident power coming from the final optical element (CPC or cone) of the BDOE. Figure 9 shows a scheme of the different parts of the system.

Dimensions of the TES tank (Figure 9.c) were defined according to criterion of thermocline tank design which recommends an aspect ratio (Height/Diameter) around 1.5. In this case, since the thermocline effect will be enhanced by the addition of an insulated divider plate inside the tank, this ratio was set to 1.55 (tank diameter of 1.25 m and height of 1.94 m). The tank is surrounded by a safety tank to recover the possible salt leakage (Fig. 9f).

The tank cover (Fig. 9b) has a 0.9 m diameter aperture to allow the entrance of the solar incident power. In order to avoid optical losses [23] and window damage due to dirt an open top container concept was implemented. The effect of sand intrusion in the tank is under study in the framework of the project.

Wall thickness of 3 mm was selected as a compromise addressing both corrosion rates (estimated from Goods et al. [24]) and energy leakage due to the thermal shortcut through the wall shell between the hot and cold salt volumes.

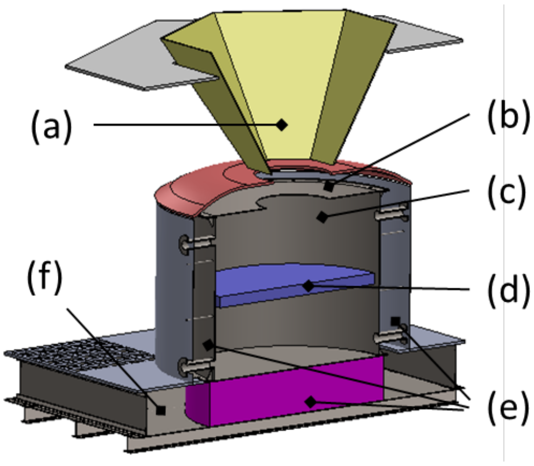

Fig. 9. Section of the FOE concept and the TES tank of the CSPonD^2 concept: (a) FOE; (b) tank cover; (c) TES tank; (d) divider plate; (e) insulation; (f) safety tank.

3.2. Operation mode description

At sunrise, the tank is completely discharged, mean salt temperature is 250ºC, and the divider plate is at its top of tank position. During the charging period salts are heated to 550ºC while the divider plate moves down with a velocity proportional to net energy accumulation within the tank. This displacement allows the increasing of the upper volume occupied by the hot salts and the decreasing of the lower volume. Cold salts moves to the upper volume through the gap between the divider plate and the tank wall. After 8 hours, the tank is completely charged and at sunset the aperture of the tank is closed with an insulated cover to avoid convective and radiative losses. Then the off-sun discharging process starts, moving the plate from bottom to top and allowing cold salts returning from the power block HX to enter through the lower penetration of the tank. During both charging and discharging processes a salt design flow rate of 3.10^{-5} m^3/s is constantly sent to the power block heat exchanger through the upper penetration of the tank.

3.3. Assessment of thermal loss

Thermal losses of the storage tank are evaluated at two different periods: the charging process, which takes place during day time (8 hours per day) and discharging process during night time (16 hours per day). In each one of those periods, the ambient temperature is taken as an average value of the meteorological data available at Masdar Institute, corresponding to 36 °C during day time and 24 °C during night time. Internal temperatures above and below the divider plate, denoted as T_{hot} and T_{cold} in the document, are considered constant at 550 °C and 250°C, respectively. Conductive losses on the side wall need to be evaluated as a transient process because of the divider plate motion along the day (from top to bottom) and night (from bottom to top). In addition, each part is insulated with different layers and thickness of insulating material presenting their own characteristics. Therefore thermal losses are evaluated at 3 different parts: the top part, corresponding to the collar of the tank with the aperture; the base, the part of the tank in contact with the ground; and the tank side wall (cf. Figure 10a).

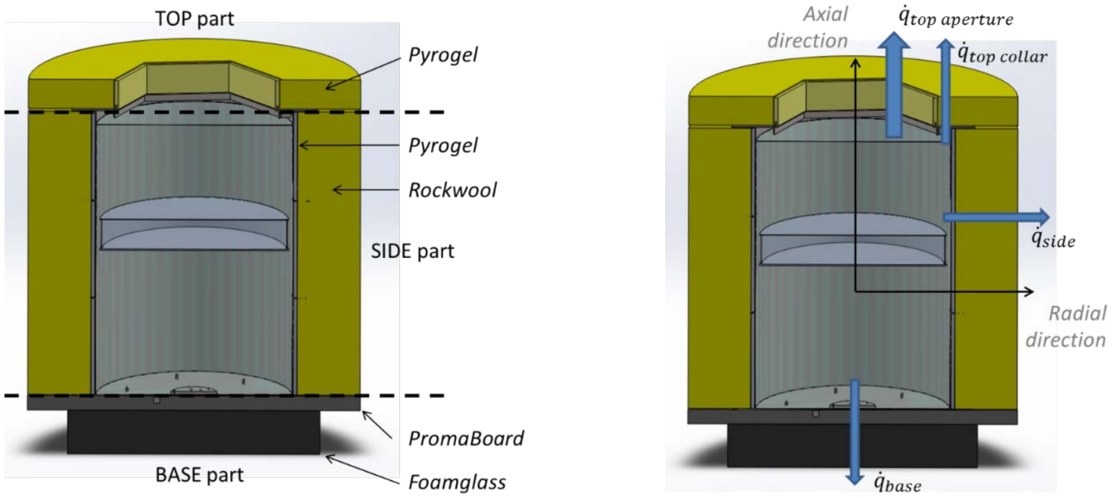

(a) (b)

Fig. 10. (a) Insulation layers installed on the tank; (b) Heat flux through the different tank parts

The heat flux is considered unidirectional and perpendicular over all the surfaces, being on axial direction on top and bottom and on radial direction on the side, as shown in Figure 10b.

- Top part

The tank top part corresponds to the collar, and the aperture of the tank allowing the penetration of the concentrated sunlight. During night time, the aperture is closed to diminish thermal losses while the system is discharged. Table 2 shows the composition of the tank top wall and the corresponding thickness and thermal conductivity.

Table 2. Thickness and thermal conductivity of the materials composing the tank top wall

	Thickness (L_i) (mm)	**Thermal conductivity (k_i) ($W.m^{-1}K^{-1}$)**
SS304L	6	21 (at 25 °C)
Pyrogel XT-E	200	0.045 (at 400 °C)

Consequently, the power loss through the tank top to the ambient during 24 hours can be calculated considering day time and night time:

$$\dot{Q}_{loss,top} = \dot{Q}_{loss,top,day} + \dot{Q}_{loss,top,night} \tag{3}$$

During night time, when the tank is closed, thermal losses are evaluated as conductive losses through an insulated horizontal plate. The top insulating layer is covered by the structural collar separated 5 cm from the insulation top, providing wind protection and reducing convective loss on the surface of the insulation. Hence, convective loss on the top are neglected.

$$\dot{Q}_{loss,top,night} = \frac{T_{hot} - T_{night}}{R_{top}} A_{top,night} \tag{4}$$

Where R_{top} is the thermal resistance, defined in Eq. 5 and $A_{top,night}$ is the total exchange area defined in Eq. 6.

$$R_{top} = \sum_i L_i / k_i \tag{5}$$

$$A_{top,night} = \pi . \left(\frac{D_{\tan k}}{2} \right)^2 \quad (6)$$

During day time, the top part can be divided in two separated areas: the aperture without any insulation and the collar, with the insulating layer described in Table 2. Then, the heat loss is defined as:

$$\dot{Q}_{loss,top,day} = \frac{T_{hot} - T_{day}}{R_{top}} . A_{collar} + A_{aperture} . h_{conv} . (T_{hot} - T_{day}) \quad (7)$$

$$A_{collar} = A_{\tan k} - A_{aperture} \quad (8)$$

For this preliminary analysis, the convective losses through the aperture of the receiver are treated as losses through an open cavity facing upward. The CPC is approximated as a 0.9 meter diameter and 1.85 meter high cylinder. The convective losses occur at the salt surface located at the bottom of the cavity with surfacetemperature set to 550 °C. The correlation of Leibfried and Ortjohann [25] is applied with an ambient temperature of 36 °C. A mean temperature between the salt surface and the CPC walls of 400 °C is assumed to calculate the Grashof number. This correlation gives a convective heat transfer coefficient of 8.2 $Wm^{-2}K^{-1}$. For these boundary conditions and cavity geometry the correlation returns a convective loss from the salt surface of 21.3 kWh. The effective emissivity of a pool of molten salt is not known however the upper bound based on $\epsilon = 1$ is 60.5 $Wm^{-2}K^{-1}$ corresponding to energy loss during an 8-hour collection period of 193.5 kWh. The minimum energy loss through the collar (not including thermal radiation) during charging and discharging processes can be determined integrating thermal losses equations for each period, respectively (Eq. 4 and 7). The values obtained from the integration are shown in Table 3.

Table 3. Thermal loses through top part of the tank calculated for day time, night time and total

	Energy loss during day (kWh)	Energy loss during night (kWh)
Conductive loss	0.55	2.32
Convective loss	21.3	n/a
Total loss	24.17	

- Base part

The tank is installed over two different insulating layers, as shown in Figure 11a. Table 4 shows the thickness and thermal conductivity of each layer, including the tank base plate.

Table 4. Thickness and thermal conductivity of the materials composing the tank base

	Thickness (L_i) (mm)	Thermal conductivity (k_i) ($W.m^{-1}.K^{-1}$)
SS304L	6	21 (at 25 °C)
Promaboard 11	100	0.1 (at 400 °C)
Foamglass HLB800	300	0.044 (at 10 °C)

The base is analysed as a flat plate with an inner salt temperature of 250 °C, while the ground temperature is set to 24 °C during both night and day. Thermal losses through the base can be expressed as in Equation 13.

$$\dot{Q}_{loss,base} = \dot{Q}_{loss,base,day} + \dot{Q}_{loss,base,night} = (2T_{cold} - T_{day} - T_{night}) . \frac{A_{base}}{R_{base}} \quad (9)$$

Where R_{base} is the thermal resistance at the base, similar to Equation 5 and A_{base} coincides with $A_{top,night}$ (Eq. 6).
The total energy loss through the base can be easily calculated by integrating Equation 9 during 24 hours, and is equal to 0.87 kWh.

- Side wall

The tank side wall is composed of the material layers listed in Table 5.

Table 5. Thickness and thermal conductivity of the materials composing the tank side wall

	Thickness (r_i) (mm)	Thermal conductivity (k_i) ($W.m^{-1}K^{-1}$)
SS304L	3	21 (at 25 °C)
Pyrogel XT-E	25	0.045 (at 550 °C)
Rockwool Spintex 342G	400	0.1 (at 400 °C)

Thermal losses from the tank side wall vary as the divider plate moves during discharging and charging processes and the relative exchange surface areas of the hot and cold salt parts change with time. Moreover thermal losses depend on the external temperature which is different for day time and night time. Consequently, energy losses from the side wall need to be calculated taking into account four main terms as shown in Equations 11 and 12.

$$\dot{Q}_{loss,side} = \dot{Q}_{loss,side,day} + \dot{Q}_{loss,side,night} \tag{10}$$

$$\dot{Q}_{loss,side,day} = \frac{T_{hot} - T_{day}}{R_{side,day,top}} + \frac{T_{cold} - T_{day}}{R_{side,day,bottom}} \tag{11}$$

$$\dot{Q}_{loss,side,night} = \frac{T_{hot} - T_{night}}{R_{side,night,top}} + \frac{T_{cold} - T_{night}}{R_{side,night,bottom}} \tag{12}$$

We make the slightly conservative assumption that thermal resistance from the side wall outer envelope (covered by a metallic sheet) to ambient is negligible compared to the insulation resistance.
As previously mentioned, thermal losses depend on the position, indicated by L in Figure 11, of the divider plate.

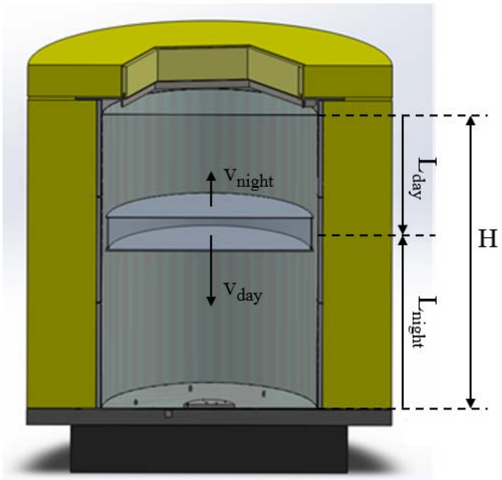

Fig. 11. Thermal losses depending on the divider plate position

Thermal resistances are written as follow:

$$R_{side,day,top} = \sum_i \frac{\ln\left(r_{i-1}/r_i\right)}{2\pi k_i . L_{day}(t)} = \frac{\sum_i \frac{\ln\left(r_{i-1}/r_i\right)}{k_i}}{2\pi . L_{day}(t)} \tag{13}$$

$$R_{side,day,bottom} = \sum_i \frac{\ln\left(r_{i-1}/r_i\right)}{2\pi k_i . \left(H - L_{day}(t)\right)} = \frac{\sum_i \frac{\ln\left(r_{i-1}/r_i\right)}{k_i}}{2\pi . \left(H - L_{day}(t)\right)} \tag{14}$$

$$R_{side,night,top} = \sum_i \frac{\ln\left(r_{i-1}/r_i\right)}{2\pi k_i . \left(H - L_{night}(t)\right)} = \frac{\sum_i \frac{\ln\left(r_{i-1}/r_i\right)}{k_i}}{2\pi . \left(H - L_{night}(t)\right)} \tag{15}$$

$$R_{side,night,bottom} = \sum_i \frac{\ln\left(r_{i-1}/r_i\right)}{2\pi k_i . L_{night}(t)} = \frac{\sum_i \frac{\ln\left(r_{i-1}/r_i\right)}{k_i}}{2\pi . L_{night}(t)} \tag{16}$$

The divider plate position $L_{day}(t)$ and $L_{night}(t)$ are defined as a function of time and divider plate velocities $v_{DP,day}$ and $v_{DP,night}$ during day time and night time, respectively.

$$L_{day}(t) = v_{DP,day} . t_{day} \tag{17}$$

$$L_{night}(t) = v_{DP,night} . t_{night} \tag{18}$$

With $v_{DP,day}$ and $v_{DP,night}$ equal to 4 mm/min and 2 mm/min, respectively.

The total energy loss during day time is calculated by integrating Equation 11 versus time, once Equations 13, 14 and 17 are included.

$$E_{loss,side,day} = \frac{2\pi\left(T_{hot} - T_{day}\right)}{\sum_i \frac{\ln\left(\frac{r_{i-1}}{r_i}\right)}{k_i}} . \int_0^8 \left(v_{DP,day} . t_{day}\right) dt_{day} + \frac{2\pi\left(T_{cold} - T_{day}\right)}{\sum_i \frac{\ln\left(\frac{r_{i-1}}{r_i}\right)}{k_i}} . \int_0^8 \left(H - v_{DP,day} . t_{day}\right) dt_{day} \qquad (19)$$

The energy loss during night can be calculated with the same procedure, obtaining as final result Equation 20.

$$E_{loss,side,day} = \frac{2\pi\left(T_{hot} - T_{night}\right)}{\sum_i \frac{\ln\left(\frac{r_{i-1}}{r_i}\right)}{k_i}} . \int_0^{16} \left(H - v_{DP,night} . t_{night}\right) dt_{night} + \frac{2\pi\left(T_{cold} - T_{night}\right)}{\sum_i \frac{\ln\left(\frac{r_{i-1}}{r_i}\right)}{k_i}} . \int_0^{16} \left(v_{DP,day} . t_{night}\right) dt_{night} \qquad (20)$$

Figures 12 and 13 shows the total energy loss during day and night (charging and discharging periods). Energy loss depends on the divider plate position. In particular, in Figure 12, when the divider plate moves from top to bottom, the energy loss within the hot part increases faster with time because the heat exchange area increases. The opposite behaviour is observed for the energy loss within the cold part.

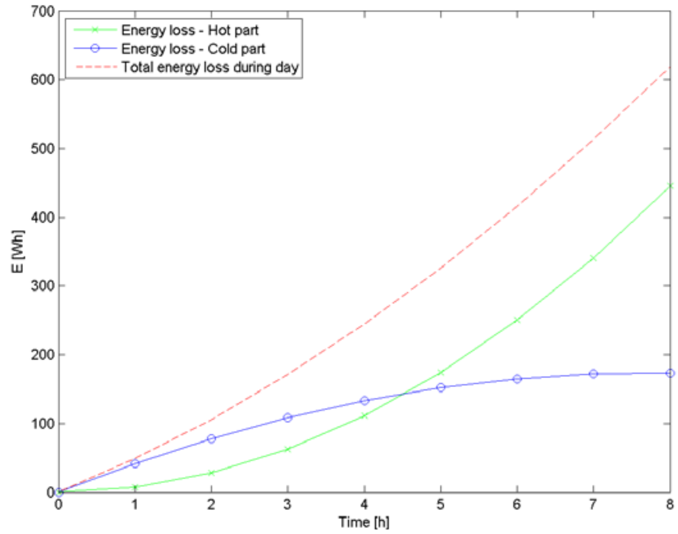

Fig. 12. Energy loss through the tank side during day (divider plate moving from top to bottom)

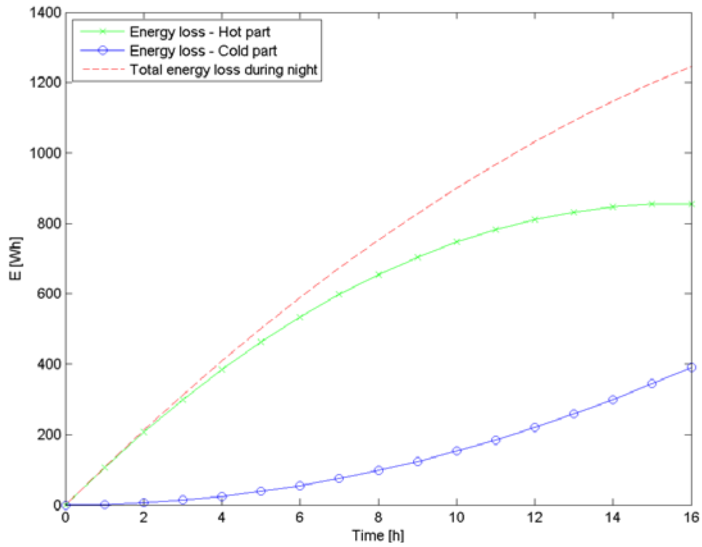

Fig. 13. Energy loss through the tank side during night (divider plate moving from bottom to top)

During the day, the total energy loss through the tank side wall tends to increase faster with time due to a larger surface of hot salt volume at 550 °C while the divider plate moves down. During night period, the total energy loss increases slower with time for the opposite reason: the upward motion of the divider plate leads to an increase of the surface of cold salt.
Table 6 shows the total energy loss within the hot and cold parts of the tank side wall during day and night periods. The energy loss during night time is higher than during day time mainly because night period is twice longer than day period. Another detail to be remarked is the energy loss within the hot part during night time is almost 3 times the one during day time. This difference comes from two factors: the different ambient temperature and divider plate velocity.

Table 6. Total energy losses through the side wall of the tank

	Day time (charging process)	**Night time (discharging process)**
Energy loss through tank hot part (kWh)	0.45	0.85
Energy loss through tank cold part (kWh)	0.17	0.39
Total energy loss through tank side wall (kWh)	1.83	

The calculated energy loss by conduction through the tank walls (top, base and side), of 26.9 kWh per day is dominated by convective loss through the aperture of 21.3 kWh. This energy loss represents 4.5 % of the total energy stored by the system of 600 kWh.

4. Conclusion and discussion

Optical simulations revealed that a 6 faceted conical design for the FOE is the best choice in terms of flux distribution uniformity, more nearly axial angular distribution of rays entering the molten salt tank and ease of manufacture and maintenance. The potential for changes in salt chemistry due to hot spots is reduced as well as the reflected flux at the molten salt surface. However for a given FOE efficiency, the cone may require a larger outlet radius, hence a larger tank aperture. A preliminary analysis focused on the conductive loss through the tank walls and on the convective loss through the aperture reveals that the total energy loss corresponds to 4.5 % of the thermal capacity. However, the thermal performance of the tank is highly dependent on the salt emissivity at 550 °C, which is not available in the literature. Ongoing experiments will provide this data and enable a better design of the FOE/tank system.

Acknowledgements

This work is funded by the Masdar Institute/MIT collaborative flagship project, grant # FR2014-000002.
Research at Masdar Institute is supported by the Government of Abu Dhabi to help fulfill the vision of the late President Sheikh Zayed bin Sultan Al Nayhan for sustainable development and empowerment of the UAE and humankind.
Masdar Institute and MIT acknowledge in alphabetic order: Dongfang Electric Corporation for designing and providing the molten salt-air heat exchanger system, National Instruments and Parker/Sunpower for donating part of instrumentation, control and motion systems, and SQM for kindly providing the nitrate salts for the prototype.

References

[1] Lund H. Renewable energy strategies for sustainable development, *Energy* 2007;32-8.
[2] Gil A et al. State of the art on high temperature thermal energy storage for power generation. Part1-Concepts, materials and modellization. *Renewable and Sustainable Energy reviews* 2010;14-25.
[3] Miro L, Oro E, Boer D, Cabeza FL. Embodied energy in thermal energy storage (TES) systems for high temperature applications, *Applied Energy* 2015;137-7.
[4] Epstein M, Segal A, Yogev, A. A molten salt system with ground base-integrated solar receiver storage tank, *Le Journal de Physique IV* 1999, 9(3).
[5] Slocum AH, et al. Concentrated solar power on demand. Solar Energy 2011;85-9.
[6] Codd DS, Carlson A, Rees J, Slocum AH. A low cost high flux solar simulator. *Solar Energy* 2010;84:2202-12.
[7] Copeland RJ. Method and apparatus for operating an improved thermocline storage unit. *U.S. Patent* 4,523,6291985.
[8] Noone CJ, Ghobeity A, Slocum AH, Tzamtzis G, Mitsos A, Site selection for hillside central receiver solar thermal plants, *Solar Energy* 2011;85:10.
[9] Codd DS, Slocum AH. Direct absorption volumetric molten salt receiver with integral storage. *Proceedings of 5th International Conference on Energy Sustainability*, Washington, DC, USA 2011.
[10] Rabl A. Tower reflector for solar power plant, *Solar Energy* 1976;18-3.
[11] Hasuike H et al. Demonstration of Tokyo Tech Beam-Down Solar Concentration Power System in 100 kW Pilot Plant. *Proceedings of 15th International Symposium on Concentrated Solar Power and Chemical Energy Technologies*, Berlin, Germany 2009.
[12] Mokhtar M, Meyers SA, Armstrong PR, Chiesa M. Performance of a 100 kWth concentrated solar beam-down optical experiement. *Journal of Solar Engineering* 2014;136:4-8.

[13] Parretta A, Antonini A. Optics of solar concentrators. Part II: Models of light collection of 3D-CPCs under direct and collimated beams. *International Journal of Optics and Applications* 2013;3(5)-31.
[14] Timinger A, Kribus A, Doron P and Ries H. Faceted concentrators optimized for homogeneous radiation. *Applied Optics* 2000;39(7):7.
[15] Jafrancesco D, Sani E, Fontani D, Mercatelli L, Sansoni P, Giannini A and Francini F. Simple methods to approximate CPC shape to preserve collection efficiency. *International Journal of Photoenergy* 2012;2012-7.
[16] Cooper T, Dähler F, Ambrosetti G, Pedretti A and Steinfeld A, Performance of compound parabolic concentrators with polygonal apertures. *Solar Energy* 2013;95-11.
[17] Segal A and Epstein M. Truncation of the secondary concentrator (CPC) as means to cost effective beam-down system. Proceedings of the ASME 3rd International Conference of Energy Sustainability, San Fransisco, CA, USA, 2009.
[18] Calvet N, Armstrong, PR, Codd, S and Slocum A. Advanced Thermal Energy Storage System Directly Charged by Concentrated Solar Power, *Flagship Research Project Full Proposal* 2014.
[19] Meyers SA, Qadir A, Mokhtar M, Rubalcaba I, Chiesa M, Armstrong PR. Development of a correlation between luminous intensity and solar flux for the beam-down tower configuration. *Proceedings of SolarPACES* 2010, Perpignan, France.
[20] Kumar, VK. *Modelling and Final Optical Element Design for Beam Down Optical Experiment*, MSME Thesis, Masdar Institute 2015
[21] Rabl A. Comparison of solar concentrators, *Solar Energy*, 1976;18:2-19.
[22] Winston R., Miñano JC and Benítez P. *Nonimaging Optics*. Elsevier Academic Press; 2005.
[23] Codd DS. Concentrated Solar Power on Demand, DS Codd thesis, PhD, Massachusetts Institute of Technology, June 2011.
[24] Goods SH, Bradshaw RW, Prairie MR, Chavez JM. Report SAND94-8211 - UC-234, March 1994.
[25] Leibfried U and Ortjohann J. Convective heat loss from upward and downward-facing cavity solar receivers: Measurements and calculations. *Journal of Solar Energy Engineering* 1995; 117:10.